

Exact quantum scars of frustrated hardcore bosons for cross-platform realizations

Zhuoli Ding¹, Ruben Verresen², and Zoe Z. Yan^{1,†}

¹ James Franck Institute and Department of Physics,
The University of Chicago, Chicago, IL 60637, USA

² Pritzker School of Molecular Engineering,
The University of Chicago, Chicago, IL 60637, USA

(Dated: March 13, 2026)

Quantum many-body scars are nonthermal states exhibiting persistent revivals in an otherwise ergodic, nonintegrable quantum system. Existing examples of exact quantum scars, however, have not yet been amenable to direct experimental demonstration. Here we show that a minimal model of hardcore bosons hopping on a π -flux ladder is sufficient to give rise to an exact scar due to kinetic frustration. The simplicity of this model makes it suitable for multiple existing quantum simulation platforms, which we illustrate with proposals for cold atom Bose-Hubbard simulators and polar molecule or Rydberg atom tweezer arrays. In these platforms, the scar lifetime can be extended by tuning experimentally accessible parameters, like the Hubbard interaction or a Floquet drive. Finally, we introduce a practical heuristic based on the energy distribution of eigenstates for systematically predicting and optimizing quantum many-body scar lifetimes. Their cross-platform realizability and long lifetimes make them well-suited for benchmarking coherence and exploring nonergodic dynamics in current and near-term quantum devices.

Introduction: Quantum many-body scars (QMBS) are intriguing exceptions to the Eigenstate Thermalization Hypothesis [1], which holds that generic many-body systems should thermalize at long times, with all observables converging to values predicted for a thermal ensemble. In contrast, scars seem to “remember” their initial conditions for anomalously long times, often leading to periodic oscillations across multiple observables even at high energy density. Scars [2–4], along with other mechanisms such as integrability [5], many-body localization [6], and Hilbert space fragmentation [7, 8], thus violate standard assumptions of quantum thermalization based on ergodic evolution. Approximate QMBS were discovered in an experiment with Rydberg atom arrays [9], spurring numerous theoretical efforts to discover and characterize these and other scars [10–33]. Despite intense theoretical efforts, observations of approximate QMBS in lattice models have been limited to a handful of efforts concentrated in the kinetically constrained PXP-type models with cold atoms and superconducting circuits [9, 34–38]. The discovery of a QMBS that is simple enough to implement across multiple quantum hardware platforms and robust enough to exhibit minimal and controllable leakage from the scar subspace could facilitate several experimental studies of quantum thermalization in many-body systems.

Here, we present a family of Hamiltonians governing hardcore bosons with nearest-neighbor hopping on a ladder, where we find special initial product states that are exact QMBS. We show that this Hamiltonian admits a tower of simple eigenstates, from which we construct the scar state, and we compute the many-body energy spectrum, entanglement entropy distribution, and perfect revivals in the many-body fidelity. Our main findings are threefold: first, to our knowledge, such a construction – a simple bosonic lattice supporting a scar due to kinet-

ically frustrated hoppings – has not been discussed previously. Second, due to the simplicity of the model, this QMBS can be built in at least two distinct types of quantum hardware platforms relevant to today’s technologies: hardcore atomic bosons in π -flux optical lattices [39] and dipolar spin-1/2 chains of Rydberg atoms [40] or polar molecules [41, 42]. Our model is therefore readily accessible in state-of-the-art experiments, an intriguing prospect given the scarcity of observations of tuneable quantum many-body scars. Third, we observe a general relationship between scar lifetimes and the energy distribution of eigenstates, giving an easily accessible heuristic that we use to characterize scar lifetimes.

Model: Exact scars in a frustrated hardcore boson ladder. We consider a ladder of hardcore bosons, denoted a_j (b_j) on the top (bottom) leg. The Hamiltonian is simply (see Fig. 1a):

$$H = -t_{\perp} \sum_j^L \left(a_j^{\dagger} b_j + \text{h.c.} \right) + t_{\parallel} \sum_j^L \left(a_j^{\dagger} a_{j+1} + \text{h.c.} \right) - t_{\parallel} \sum_j^L \left(b_j^{\dagger} b_{j+1} + \text{h.c.} \right),$$

where the hopping t_{\parallel} along the legs and t_{\perp} along the rungs can always be taken to be non-negative by absorbing a phase into the bosons. There are N total number of sites, where $L = N/2$ is the length of the ladder. We note that by the Peierls substitution method [43], this is equivalent to a model of hardcore bosons hopping in a magnetic field with π -flux per plaquette.

These hardcore bosons are fully frustrated: there is destructive interference around a plaquette. To see this on the level of a single plaquette of four sites, let us consider the time-evolution from a special initial state $|\psi\rangle = \begin{vmatrix} 0 & 0 \\ 1 & 1 \end{vmatrix}$ of a half-filled system with all bosons on the bottom leg.

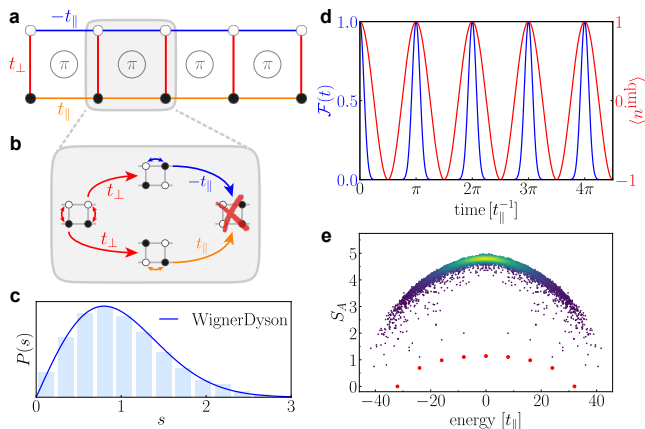


FIG. 1. **Exact quantum many-body scars in a hardcore boson ladder with π -flux per plaquette.** (a) Illustration of a $L = 5$ ladder with hardcore bosons tunneling as $-t_{\parallel}$ in the top leg, t_{\parallel} in the bottom leg, and t_{\perp} on the rungs. Our QMBS state is pictured as a filled bottom leg (black circles) and an unoccupied top leg. The destructive interference from tunneling around one square plaquette leads to a π -flux. (b) In one plaquette, destructive interference of the initial state (left) evolving into a final, non-scar configuration (right) is illustrated, via two potential paths (top and bottom) whose amplitudes carry a relative π phase shift. (c) The nearest-neighbor energy level spacing distribution of the model defined in Eq. 1 for a $L = 9$ ladder with a small second-nearest neighbor hopping that preserves the scar (see End Matter for details). The spacings follow a Wigner-Dyson distribution (blue curve), indicating non-integrability of the model. (d) Dynamics of the scar, showing the time-evolution of the many-body fidelity $\mathcal{F}(t)$ (left axis, blue line) and the observable $\langle n^{\text{imb}} \rangle$ (right axis, red line) for a $L = 10$ ladder with $t_{\perp} = t_{\parallel}$. (e) The entanglement entropy S_A of the ladder split across the middle as a function of energy for $L = 8$ ladder, calculated at half-filling. The scar states are in red.

Time-evolving under Eq. 1 does not allow for two bosons to occupy the same rung, like $\begin{pmatrix} 0 & 1 \\ 0 & 1 \end{pmatrix}$. Indeed, the π -flux implies destructive interference that cancels out the two pathways (see Fig. 1b). This motivates the definition of our QMBS, extending the system beyond a simple square plaquette to a $2 \times L$ ladder, as the product state with all bosons in the bottom leg $|\psi_{\text{scar}}\rangle = \begin{pmatrix} 0 & 0 & 0 & \dots \\ 1 & 1 & 1 & \dots \end{pmatrix}$. We will prove this is an exact scar, which we furthermore numerically demonstrate through direct time-evolution. While frustration-based scars have appeared in projector-embedded models [44, 45], our mechanism relies instead on kinetic frustration without invoking frustration-free degeneracies or flat bands [46].

Spectrum-Generating Algebra: A useful way to define QMBS is through the explicit construction of a tower of special eigenstates using a ladder-operator [18, 23, 24] which generates ‘ferromagnetic scar states’ [47, 48]. On each rung, we define $|d^{\pm}\rangle = \frac{1}{\sqrt{2}}(|\begin{smallmatrix} 1 \\ 0 \end{smallmatrix}\rangle \pm |\begin{smallmatrix} 0 \\ 1 \end{smallmatrix}\rangle)$. One can verify that the product state $|\psi_0\rangle = |d^- d^- \dots d^- \rangle$ is an eigenstate of H due to the kinetic frustration. We then

introduce a creation operator

$$J^+ = \sum_{j=1}^L |d_j^+\rangle \langle d_j^-|. \quad (2)$$

Repeated application of J^+ on $|\psi_0\rangle$ generates a sequence of eigenstates $|\psi_n\rangle \propto (J^+)^n |\psi_0\rangle$. The set of states generated in this way forms a subspace, which we refer to as the scarring subspace, $\mathcal{H}_{\text{scar}} = \text{span}\{|\psi_0\rangle, |\psi_1\rangle, \dots, |\psi_L\rangle\}$. Importantly, this subspace has dimension $L + 1$, and the eigenstates are equally spaced in energy by $\Delta E = 2t_{\perp}$. Consequently, any state within $\mathcal{H}_{\text{scar}}$ undergoes perfectly periodic time evolution and revives exactly after a fixed period of π/t_{\perp} . One can show that $|\psi_{\text{scar}}\rangle$ can be written as a coherent superposition of all the scar eigenstates $|\psi_n\rangle$ and therefore this construction can provide an explicit explanation of the scarred nature of this special initial state.

To quantify a figure of merit for the QMBS, a common benchmark is the many-body fidelity of the initial state under time evolution, $\mathcal{F}(t) \equiv |\langle \psi_{\text{scar}}(t=0) | \psi_{\text{scar}}(t) \rangle|^2$. However, this observable is difficult to measure experimentally. Instead, we define another QMBS figure-of-merit: the average imbalance $\langle n^{\text{imb}} \rangle = \frac{1}{L} \sum_{j=1}^L n_j^{\text{imb}}$, with imbalance defined as $n_j^{\text{imb}} = n_j^{\text{top}} - n_j^{\text{bot}}$. The imbalance is accessible to measurements in existing quantum simulators, as will be discussed in detail in later sections. We numerically solve the model by performing exact diagonalization using QuSpin [49]. We first show the distribution of energy level spacings in a symmetry sector (Fig. 1c), which follows the Wigner-Dyson distribution rather than Poissonian, indicating nonintegrability of the model where we added a small second-nearest neighbor hopping to minimize finite-size effects (see End Matter). Fig. 1d shows the time evolution of $\mathcal{F}(t)$ and averaged imbalance $\langle n^{\text{imb}} \rangle$, where the exact revival is confirmed by full-contrast many-body oscillations that persist forever. Fig. 1e shows the distribution of bipartite entanglement entropy. The scarring subspace is highlighted using red dots, showing entanglement entropy much lower than that of generic thermal states (details in End Matter). Taken together, the energy distribution, the periodic revivals, and the entanglement spectrum show this model has distinct QMBS characteristics.

Experimental implementations. Our simple model finds wide application across several hardware platforms, all accessible with today’s technology. We highlight two classes of quantum simulators: (1) hardcore atomic bosons in optical lattices in the presence of artificial magnetic fields, and (2) spin-1/2 particles interacting under the dipolar XY (spin-exchange) Hamiltonian.

Hardcore bosons in π -flux lattices. Ultracold atoms in optical lattices have become a paradigm for analog quantum simulation [50]. Bosonic atoms are commonly used in state-of-the-art quantum gas microscopes [51], where site-resolved population dynamics are probed in high-fidelity snapshot images. Here, we provide a concrete roadmap to realize our model using spinless bosons in

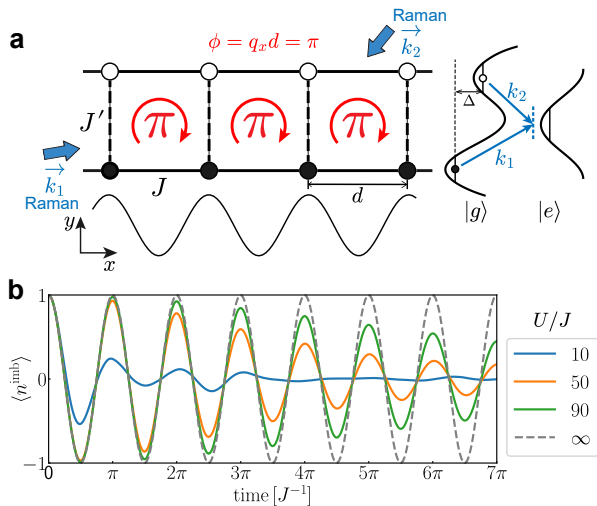


FIG. 2. **Implementation of the model using ultra-cold bosonic atoms experiencing an artificial magnetic field.** (a) The approximate QMBS comprises a half-filled boson ladder (black circles). The lattice setup includes a uniform sinusoidal potential in x and a staggered double-well in y , with energy offset Δ and lattice constant d . A pair of Raman lasers (blue arrows) with wavevectors $\mathbf{k}_1, \mathbf{k}_2$ induce photon-assisted tunneling in y via an optical two-photon transition using the atom’s excited state $|g\rangle \rightarrow |e\rangle$. Nearest neighbor complex- and real-valued tunnelings with magnitudes J', J , respectively, couple the y and x directions. With appropriate choice of Raman laser detunings and angles, each plaquette has an effective π -flux. (b) Dynamics of the scar for $L = 7$, showing $\langle n^{\text{imb}} \rangle$ for various $U/|J| = U/|J'|$. For infinite interactions, the bosons obey a hardcore constraint, leading to persistent revivals.

an optical lattice within the Bose-Hubbard regime. The protocol is inspired by proposals [52–54] and past experiments [55–60] for creating effective magnetic fields with Raman lasers. The geometry we consider is pictured in Fig. 2a: a ladder in which bosons hop along one leg (in the x -axis) in a sinusoidal potential with periodicity d , and between legs (in y) within a ‘tilted’ double-well system. The two legs experience an energy offset Δ much larger than the nearest-neighbor hoppings t , which are equal for inter- and intra-leg tunneling. Therefore, inter-leg hopping is normally suppressed; however, a pair of Raman lasers with wavevectors $\mathbf{k}_1, \mathbf{k}_2$ ($|\mathbf{k}_2| \approx |\mathbf{k}_1|$) can provide photo-assisted tunneling between legs [55, 56]. Experimentally, a Hamiltonian similar to Eq. 1 is realized when the Raman lasers experience a frequency difference $\hbar(\omega_1 - \omega_2) = \Delta$, creating a running wave along the vector $\mathbf{q} = \mathbf{k}_1 - \mathbf{k}_2$. In this way, spatially-dependent complex tunneling amplitudes J and $J' = |J'|e^{i\phi(\mathbf{r})}$ can be engineered along x and y , respectively, leading to an Aharonov-Bohm phase $\phi = q_x d$ when a particle tunnels around a square plaquette, which can be tuned to π with Raman laser parameters. Doubly-occupied sites experience a Hubbard repulsion energy, U , which blocks multiparticle occupancies. The effective model govern-

ing the system under the tight-binding approximation is the Harper-Hofstadter-Bose-Hubbard (HHBH) Hamiltonian [43, 61] [see Supplement]. These main experimental components have been demonstrated on cold atom simulators [55–60].

The approximate QMBS is realized by initializing L bosons on one leg of the $2 \times L$ ladder (see Fig. 2a) – a half-filled Mott insulating state that has been demonstrated for state preparation in past experiments [60]. For hardcore bosons, the QMBS manifests as the population dynamically changing from all bosons in the bottom leg to all bosons in the top leg. This oscillation repeats indefinitely for a perfect scar, as shown in the dashed line of Fig. 2b. The hardcore boson constraint is approached by working in a regime where $U/|J'|, U/|J| \gg 1$. At intermediate or weak Hubbard repulsion, the initial state will leak into states in the Hilbert space with double occupancies, causing decay of the scar observable (see Fig. 2b). A quantum gas microscope making use of species with magnetic Feshbach resonances for tuning U may be able to access the relevant strongly-interacting regimes capable of probing the QMBS with long-lived revivals.

Dipolar spin chains. Beyond hardcore bosons in optical lattices, the QMBS can be implemented in a dipolar spin-1/2 zig-zag chain (Fig. 3), with a boson mapped to $|\uparrow\rangle$ and an empty site mapped to $|\downarrow\rangle$. The spins can be encoded in two rotational levels of a polar molecule or two orbital angular momentum states of a Rydberg atom [see Supplement], and motion of the particles is frozen. The system evolves under the lattice spin-exchange Hamiltonian [62–64]

$$\hat{H}_{\text{SE}} = \sum_{i>j} \frac{J_{ij}}{2} \left(\hat{S}_i^+ \hat{S}_j^- + \hat{S}_i^- \hat{S}_j^+ \right) \quad (3)$$

where S^+, S^- are the spin-1/2 raising and lowering operators. The exchange interaction is given by the dipolar coupling $J_{ij} = V_{\text{ddi}}(\mathbf{r}_i - \mathbf{r}_j) = \frac{d^2(1-3\cos^2\theta)}{4\pi\epsilon_0|\mathbf{r}_i - \mathbf{r}_j|^3}$, where θ denotes the angle between the dipoles’ quantization axis and their separation and d is the electric dipole moment. Instead of a ladder geometry, we “twist” every other rung to obtain the zig-zag chain of Fig. 3a-b, and the tunnel-couplings of Eq. 1 become the exchange interactions J_{ij} . The carefully chosen angles in the chain are crucial to recover the phenomenology of the QMBS. By the choice of the zig-zag angles α, β and the quantization axis direction (which can be out of plane), the diagonal coupling terms J_{13} and J_{02} are equal in magnitude but opposite in sign, fulfilling the kinetic frustration condition of destructive interference in analogy to the model in Fig. 1a. Crucially, the undesired interactions J_{03}, J_{12} can be avoided using the node in the coupling at $\theta = \cos^{-1} \sqrt{1/3}$ [see Supplement for the full set of parameters].

The QMBS state is prepared in an initial product state with L sites excited to $|\uparrow\rangle$ in an $2L$ -length chain (see Fig. 3b): $|\psi_{\text{scar}}\rangle = |\downarrow\uparrow\downarrow\uparrow\downarrow\dots\rangle$ with $\langle n^{\text{imb}} \rangle = 1$. Fig. 3c shows the evolution of $\langle n^{\text{imb}} \rangle$ for a zig-zag $L = 10$ chain with $\alpha = 34^\circ, \beta = 32.45^\circ$ and the quantization axis 30°

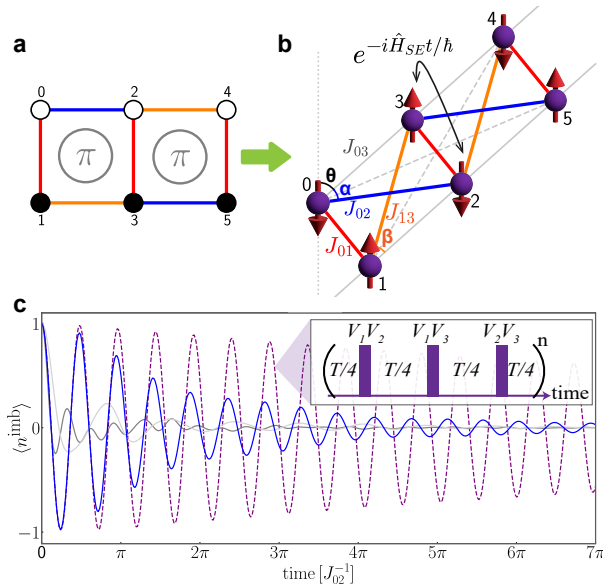


FIG. 3. **Implementation of the model using dipolar spin-1/2 degrees of freedom.** (a) Transformation of the two-leg hardcore boson ladder of Fig. 1a into a dipolar zig-zag chain. Rydberg atoms or polar molecules trapped in optical tweezers form a spin-1/2 system spanned by two internal states ($|\downarrow\rangle, |\uparrow\rangle$), and they interact under the spin-exchange Hamiltonian \hat{H}_{SE} . (b) Relevant parameters of the dipolar zig-zag chain with six sites pictured. Intra-rung interactions (in red) J_{01} couple $n, n+1$ with n even. Next-nearest-neighbor couplings (in solid grey) are zero at the magic angle of $1 - 3\cos^2\theta = 0$. Blue and orange lines indicate J_{02} and J_{13} , with angles of α and β with respect to the zig-zag chain, respectively. Longer-range couplings are indicated in dashed grey lines. (c) Dynamics of the dipolar QMBS showing $\langle n^{\text{imb}} \rangle$ (in blue). The scar lifetime can be extended by Floquet-engineering (in purple) to cancel the longer-range couplings, with the Floquet pulse sequence given in the inset (see text for details). The long-lived scar exists in contrast to typical thermal states (in grey), which show fast decay of oscillations (see End Matter for numerical details).

out of the plane. Compared to a typical thermal state, $|\psi_{\text{scar}}\rangle$ demonstrates long-lived emergent many-body oscillations [Fig. 3c]. Unlike the exact scar of the Hamiltonian in Eq. 1, here, the oscillations decay over time due to the presence of longer-range dipolar couplings (shown as grey dashed lines in Fig. 3b). The resulting revivals have a quality factor comparable to the PXP model for a similar system size and implemented with Rydberg atom arrays [9].

To further stabilize the scar dynamics, we use simple Floquet engineering [34, 65] to cancel the longer-range (grey dashed) interactions, which are the dominant errors in the dipolar chain. Considering a π rotation on rung $j \in [1, L]$, we define $V_j \equiv \exp(i\pi(a_j^\dagger a_j + b_j^\dagger b_j))$ in the hardcore boson ladder notation. Let $U(t) = \exp(-it\hat{H}_{SE})$ denote the time evolution. We define the Floquet unitary over a period T , defined for a unit cell of four rungs: $U_F(T) = U(\frac{T}{4})V_1V_2U(\frac{T}{4})V_1V_3U(\frac{T}{4})V_2V_3U(\frac{T}{4})$. This Flo-

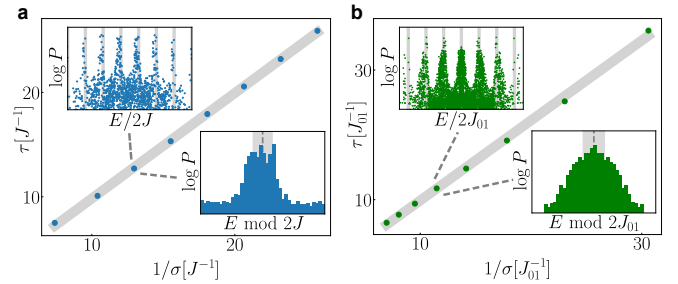


FIG. 4. **Predicting the thermalization time of an approximate QMBS from its energy distribution.** Due to experimental limitations, the approximate QMBS states exhibit finite lifetimes τ in both the π -flux boson ladder taking $|J'| = |J|$ (a) and the dipolar spin chain (b), where each point is a different parameter – varying the Hubbard U or the angles for the dipolar zig-zag chain, respectively [see Supplement for details]. The top left insets show the eigenenergy distribution for one such Hamiltonian, revealing a spread compared to an exact scar’s equally spaced tower of eigenstates (grey lines). From this, we extract the fractional energy distribution (bottom right insets), fitting the width 2σ given by the grey shaded area. Here P is the weighted probability distribution of the overlap between QMBS state and many-body eigenstates. There is a clear linear relationship between τ and $1/\sigma$ for both models, allowing us to optimize the scar lifetime using the energy distributions.

quet operator cancels out the longer-range couplings over four rungs that reduce the scar lifetime, while preserving the nearest-neighbor couplings J_{01} and the relationship $J_{02} = -J_{13}$, when averaged over many periods T [see End Matter]. Fig. 3c shows the scar observable with and without Floquet driving, demonstrating that the cancellation of longer-range couplings leads to enhanced stability of the QMBS. One can similarly systematically cancel higher-order terms if desired.

Our proposal of the dipolar XY quantum many-body scar can be implemented in existing Rydberg and polar molecule quantum simulators. In dipolar Rydberg chains [40, 66–71], nearest-neighbor couplings of $J \approx h \times 0.1 - 10\text{MHz}$ are achievable. Decoherence primarily stems from finite lifetimes and spreading of position distributions due to thermal motion. An estimate of these effects using values reported in Ref. [70] show that the scar visibility is robust against this leading disorder effect for certain parameter regimes [see Supplement]. In polar molecules, the spin-exchange Hamiltonian has been studied in lattice [72–74] and optical tweezer [75–78] systems, and extension to our model with a dipolar zig-zag chain is straightforward.

Connection between scar lifetimes and energy distributions: In these experimental realizations, imperfections (finite Hubbard interaction or the longer-range dipolar interactions) lead to a decay of the scar dynamics. In searching for parameters that maximize scar lifetimes, we find a useful connection between the lifetime and the energy distribution of the eigenstates. Recall that an exact

QMBS state (with infinite revivals) can be constructed from a tower of eigenstates that are equally spaced in energy by $\Delta E = 2t_{\perp}$ (i.e., $2|J'|$ in the Bose-Hubbard ladder and $2J_{01}$ in the dipolar spin chain). With imperfections, the spectral weight of the approximate QMBS state remains concentrated near these equally spaced energies [see Fig. 4], but the spread of this distribution leads to decay of the revivals. To quantify this, we first compute the overlap of the approximate QMBS state with the many-body eigenstates. For each contributing eigenstate, we define the *fractional energy* as $E \bmod 2J'$ – the minimal distance to the nearest eigenenergy of the exact scar spectrum. The inset of Fig. 4 shows the resulting probability distribution, and the energy width σ is its standard deviation. We find that this energy width is inversely proportional to the lifetime of the approximate QMBS state [Fig. 4]. We extract the approximate scar’s lifetime τ for a variety of experimental parameters by fitting the scar evolution to an envelope function $\sim \exp(-t/\tau)$ [see Supplement]. The linear relationship between τ and $1/\sigma$ suggests a strategy for optimizing scar dynamics. By directly computing the spectral width associated with a given initial state and Hamiltonian, one can assess the robustness of scarring without resorting to long-time dynamical simulations, and we expect that this easily calculable heuristic could be used widely across different scarred systems. We used this fitting-free approach to study how the scar lifetime depends on the perturbations away from the ideal scar, observing τ to scale with the inverse perturbation strength for these two examples [see Supplement for further results].

Conclusion and outlook: We have demonstrated that kinetic frustration is sufficient to give rise to an exact scar, as realized in a simple hardcore boson model which is experimentally accessible to many current quantum simulators. Though experimental limitations cause leakage out of the scar subspace and eventual thermalization, we show that tuning experimental parameters – the Hubbard repulsion or Floquet engineering – can bring the system parametrically close to the ideal exact scar. We have developed a heuristic for optimizing scar lifetimes, which we expect is broadly applicable to other scarred systems, and our observation that the scar lifetime scales with the inverse perturbation strength deserves further study in light of other parametric observations in the literature [79]. Our proposal could lead to the implementation of long-lived QMBS states, which could serve as a useful resource for storing long-lived quantum information [3], generating entangled states for quantum metrology [80], and benchmarking coherence in quantum simulators across multiple platforms.

We would like to thank Thomas Iadecola, Olexei Motrunich, Maksym Serbyn and Michael Zaletel for interesting discussions. Z.Y. acknowledges support from the David and Lucile Packard Foundation (2024-77404), the Air Force Young Investigator Program (FA9550-25-1-0360), and the Neubauer Family Assistant Professors Program.

† Email: zzyan@uchicago.edu

END MATTER

A. Spectrum Generating Algebra

The method of the spectrum generating algebra (SGA) states that for an eigenstate $|\psi_0\rangle$ with energy E_0 , if the commutator between a creation operator J^+ and Hamiltonian H_{SG} satisfies $[H_{\text{SG}}, J^+] = \omega J^+$ ($\omega \neq 0$), then $|\psi_n\rangle = (J^+)^n |\psi_0\rangle$ is also an eigenstate with energy $E_0 + n\omega$ as long as the eigenstate is nonzero. We find that our model can be described by the notion of a restricted SGA [18, 23, 24], which only requires that the commutation relationship holds within the scarred subspace.

Following Ref. [4], we introduce generators $J^{\pm} = \sum_{j=1}^L |d_j^{\pm}\rangle \langle d_j^{\mp}|$ and $J^z = \sum_{j=1}^L (|d_j^+\rangle \langle d_j^+| - |d_j^-\rangle \langle d_j^-|)$. The Hamiltonian can be written into three parts:

$$H = H_{\text{sym}} + H_{\text{SG}} + H_A, \quad (4)$$

H_{sym} commutes with J^{\pm} and J^z , H_{SG} satisfies $[H_{\text{SG}}, J^{\pm}] = \pm\omega J^{\pm}$ which lifts the degenerate multiplets of H_{sym} . The final term H_A does not commute with J^{\pm} , J^z , but annihilates the scar states $H_A |\psi_n\rangle = 0$. Defining $|d^0\rangle = |0\rangle$, $|d^1\rangle = |1\rangle$, for the exact scar (Eq. 1), H_{SG} is

$$H_{\text{SG}} = - \sum_{j=1}^L t_{\perp} \left(|d_j^+\rangle \langle d_j^+| - |d_j^-\rangle \langle d_j^-| \right), \quad (5)$$

H_A is

$$H_A = t_{\parallel} \sum_{j=1}^{L-1} \left(|d_j^0 d_{j+1}^-\rangle \langle d_j^+ d_{j+1}^0| + |d_j^- d_{j+1}^0\rangle \langle d_j^+ d_{j+1}^+\rangle \right. \\ \left. - |d_j^- d_{j+1}^1\rangle \langle d_j^+ d_{j+1}^+| - |d_j^1 d_{j+1}^-\rangle \langle d_j^+ d_{j+1}^1| \right) + \text{h.c.} \quad (6)$$

We note that because the rung hopping (H_{SG}) is not a single-site term, the persistent oscillations are also accompanied by nonzero entanglement oscillations, which physically corresponds to the particle on a given rung oscillating between the two sites as a periodic function of time. This is distinct from the mechanism discussed in Refs. 48 and 81, where in a variety of examples the energetics is determined by an effective *single-site* Hamiltonian which thereby gives completely frozen entanglement dynamics.

B. Floquet Engineering for Dipolar Model

While Floquet engineering has been used to improve scar lifetimes [34, 65], the mechanism is often non-trivial.

In contrast, the knowledge of the ideal scar in our exact model allows for a straightforward pulse sequence that systematically cancels out the longer-range terms which would otherwise spoil the exactness. For instance, consider the pulse sequence from the main text:

$$\begin{aligned} U_F(T) &= U\left(\frac{T}{4}\right) V_1 V_2 U\left(\frac{T}{4}\right) V_1 V_3 U\left(\frac{T}{4}\right) V_2 V_3 U\left(\frac{T}{4}\right) \\ &= U\left(\frac{T}{4}\right) \left(V_1 V_2 U\left(\frac{T}{4}\right) V_2^\dagger V_1^\dagger \right) \\ &\quad \times \left(V_2 V_3 U\left(\frac{T}{4}\right) V_3^\dagger V_2^\dagger \right) U\left(\frac{T}{4}\right) \end{aligned} \quad (7)$$

where V_j denotes a π -pulse on the j 'th rung. A hopping term is flipped by conjugating with the V_j 's if and only if it overlaps with only *one* site involved in the pulse. This way, we see that the rung hoppings t_\perp all add up, whereas the horizontal hoppings t_\parallel get partially suppressed by a factor of two. Crucially, the second-nearest-neighbor hoppings along the horizontal direction are toggled half of the times, thereby completely canceling out in this Floquet sequence.

C. Generalized Definition of Imbalance

For generic product states, we generalize the definition of imbalance: for each individual site as i , define $\sigma_i^z = 2n_i - 1$, the averaged imbalance is defined as

$$\langle n_{\text{imb}} \rangle = \frac{1}{N} \sum_{i=0}^N \langle \sigma_i^z(t) \rangle \langle \sigma_i^z(0) \rangle, \quad (8)$$

where N is the total number of sites.

D. Numerical Details

Details for Fig. 1. In Fig.1c, we compute the nearest-neighbor level spacing distribution within the fully symmetry-resolved sector, for a chain of $L = 9$ with open boundary conditions and $t_\perp = t_\parallel$. Spin-flip symmetry, $S_z = 0$ conservation, and spatial reversal symmetry are taken into account.

To obtain a cleaner quantum chaotic behavior, we introduce next-nearest-neighbor tunneling in the horizontal axis, with t_{nn} in the top leg and $-t_{\text{nn}}$ in the bottom leg. These additional terms preserve the conditions required for the existence of the scar state, while suppressing finite-size effects. The strength of the long-range hopping is chosen as $t_{\text{nn}} = 0.1t_\perp$. After symmetry reduction, the effective Hilbert space dimension is 7272. The resulting level spacing statistics yield an average gap ratio $r = 0.5291$, in close agreement with the Wigner-Dyson prediction $r_{\text{WD}} = 0.5295$. Further calculations indicating non-integrability of our model are presented in the supplement.

For the entanglement entropy in Fig. 1e, we used the same hopping strength with $L = 8$ in $N_z = L$ sector, where N_z is the total number of bosons. In Fig. 1d, the time evolution of fidelity and imbalance are shown for a $L = 10$ chain, with the same model parameters as before.

Details for Fig. 2. For Fig. 2b, since the onsite interaction strength U is much larger than the tunneling, we restrict the local bosonic occupation to $n_i \leq 2$ and choose $L = 7$ with open boundary conditions.

Details for Fig. 3. In Fig. 3c, we show the time evolution of the generalized imbalance of two representative product states. $|\psi_{\text{thermal},1}\rangle = \text{site index} \begin{bmatrix} 0 & 3 & 4 & \dots \\ 1 & 2 & 5 & \dots \end{bmatrix} = \begin{bmatrix} 0 & 0 & 0 & \dots \\ 1 & 1 & 1 & \dots \end{bmatrix}$ and $|\psi_{\text{thermal},2}\rangle = \text{site index} \begin{bmatrix} 0 & 3 & 4 & \dots \\ 1 & 2 & 5 & \dots \end{bmatrix} = \begin{bmatrix} 1 & 0 & 0 & \dots \\ 1 & 0 & 1 & \dots \end{bmatrix}$ correspond to grey and light-grey curves, respectively, using Eq. 8.

Floquet engineering parameters in Fig. 3c. We used a Floquet period of $T = \pi/J_{01}$ and assumed infinitely short pulse durations V_i . We have separately confirmed that for pulse durations $\sim \frac{T}{20}$, the finite-pulse window has no appreciable effect on the scar quality.

Details for Fig. 4. In Fig. 4a, τ and σ are calculated with $L = 7$ chain and $n_i \leq 2$, with $U/|J| = U/|J'|$ in the range of $[30, 100]$. In Fig. 4b, τ is fitted from the time evolution of a $L = 10$ chain while σ is calculated from exact diagonalization of a $L = 8$ chain. The quantization axis is 30° out of the plane and α is varied in the range of $[26, 40]$ degrees, corresponding to J_{02}/J_{01} in the range of $[0.2, 0.7]$. The y axis of top left inset ranges from $[10^{-7}, 0.2]$ while the y scale of bottom left inset is $[10^{-4}, 1]$. The fitting details can be found in the supplement.

[1] L. D'Alessio, Y. Kafri, A. Polkovnikov, and M. Rigol, *Advances in Physics* **65**, 239 (2016).
[2] C. J. Turner, A. A. Michailidis, D. A. Abanin, M. Serbyn, and Z. Papić, *Nature Physics* **14**, 745 (2018).
[3] M. Serbyn, D. A. Abanin, and Z. Papić, *Nature Physics* **17**, 675 (2021).
[4] A. Chandran, T. Iadecola, V. Khemani, and R. Moessner, *Annual Review of Condensed Matter Physics* **14**, 443 (2023).
[5] M. Rigol, V. Dunjko, V. Yurovsky, and M. Olshanii,

Phys. Rev. Lett. **98**, 050405 (2007).
[6] R. Nandkishore and D. A. Huse, *Annu. Rev. Condens. Matter Phys.* **6**, 15 (2015).
[7] P. Sala, T. Rakovszky, R. Verresen, M. Knap, and F. Pollmann, *Phys. Rev. X* **10**, 011047 (2020).
[8] V. Khemani, M. Hermele, and R. Nandkishore, *Phys. Rev. B* **101**, 174204 (2020).
[9] H. Bernien, S. Schwartz, A. Keesling, H. Levine, A. Omran, H. Pichler, S. Choi, A. S. Zibrov, M. Endres, M. Greiner, *et al.*, *Nature* **551**, 579 (2017).

- [10] C. J. Turner, A. A. Michailidis, D. A. Abanin, M. Serbyn, and Z. Papić, *Phys. Rev. B* **98**, 155134 (2018).
- [11] S. Choi, C. J. Turner, H. Pichler, W. W. Ho, A. A. Michailidis, Z. Papić, M. Serbyn, M. D. Lukin, and D. A. Abanin, *Phys. Rev. Lett.* **122**, 220603 (2019).
- [12] N. Shiraishi and T. Mori, *Physical Review Letters* **119**, 030601 (2017).
- [13] T. Mori and N. Shiraishi, *Physical Review E* **96**, 022153 (2017).
- [14] S. Ok, K. Choo, C. Mudry, C. Castelnovo, C. Chamon, and T. Neupert, *Physical Review Research* **1**, 033144 (2019).
- [15] Y. Kuno, T. Mizoguchi, and Y. Hatsugai, *Physical Review B* **102**, 241115 (2020).
- [16] K. Omiya and M. Müller, *Physical Review A* **107**, 023318 (2023).
- [17] D. K. Mark, C.-J. Lin, and O. I. Motrunich, *Physical Review B* **101**, 195131 (2020).
- [18] S. Moudgalya, N. Regnault, and B. A. Bernevig, *Physical Review B* **102**, 085140 (2020).
- [19] N. O’Dea, F. Burnell, A. Chandran, and V. Khemani, *Physical Review Research* **2**, 043305 (2020).
- [20] K. Pakrouski, P. N. Pallegar, F. K. Popov, and I. R. Klebanov, *Physical Review Letters* **125**, 230602 (2020).
- [21] J. Ren, C. Liang, and C. Fang, *Physical Review Letters* **126**, 120604 (2021).
- [22] J.-J. Feng, B. Zhang, Z.-C. Yang, and Q. Zhuang, *npj Quantum Information* **11**, 42 (2025).
- [23] S. Moudgalya, N. Regnault, and B. A. Bernevig, *Physical Review B* **98**, 235156 (2018).
- [24] M. Schecter and T. Iadecola, *Physical Review Letters* **123**, 147201 (2019).
- [25] S. Moudgalya, B. A. Bernevig, and N. Regnault, *Reports on Progress in Physics* **85**, 086501 (2022).
- [26] F. Yang, M. Magoni, and H. Pichler, *arXiv preprint arXiv:2506.10806* (2025).
- [27] S. Moudgalya and O. I. Motrunich, *Phys. Rev. X* **14**, 041069 (2024).
- [28] C.-J. Lin and O. I. Motrunich, *Phys. Rev. Lett.* **122**, 173401 (2019).
- [29] D. K. Mark and O. I. Motrunich, *Phys. Rev. B* **102**, 075132 (2020).
- [30] K. Pakrouski, P. N. Pallegar, F. K. Popov, and I. R. Klebanov, *Phys. Rev. Res.* **3**, 043156 (2021).
- [31] C. M. Langlett, Z.-C. Yang, J. Wildeboer, A. V. Gorshkov, T. Iadecola, and S. Xu, *Phys. Rev. B* **105**, L060301 (2022).
- [32] J.-Y. Desaulles, A. Hudomal, C. J. Turner, and Z. Papić, *Phys. Rev. Lett.* **126**, 210601 (2021).
- [33] M. Kunimi, T. Tomita, H. Katsura, and Y. Kato, *Phys. Rev. A* **110**, 043312 (2024).
- [34] D. Bluvstein, A. Omran, H. Levine, A. Keesling, G. Semeghini, S. Ebadi, T. T. Wang, A. A. Michailidis, N. Maskara, W. W. Ho, *et al.*, *Science* **371**, 1355 (2021).
- [35] I.-C. Chen, B. Burdick, Y. Yao, P. P. Orth, and T. Iadecola, *Phys. Rev. Res.* **4**, 043027 (2022).
- [36] G.-X. Su, H. Sun, A. Hudomal, J.-Y. Desaulles, Z.-Y. Zhou, B. Yang, J. C. Halimeh, Z.-S. Yuan, Z. Papić, and J.-W. Pan, *Phys. Rev. Res.* **5**, 023010 (2023).
- [37] P. Zhang, H. Dong, Y. Gao, L. Zhao, J. Hao, J.-Y. Desaulles, Q. Guo, J. Chen, J. Deng, B. Liu, *et al.*, *Nature Physics* **19**, 120 (2023).
- [38] L. Zhao, P. R. Datla, W. Tian, M. M. Aliyu, and H. Loh, *Phys. Rev. X* **15**, 011035 (2025).
- [39] N. R. Cooper, J. Dalibard, and I. B. Spielman, *Rev. Mod. Phys.* **91**, 015005 (2019).
- [40] A. Browaeys and T. Lahaye, *Nature Physics* **16**, 132 (2020).
- [41] T. Langen, G. Valtolina, D. Wang, and J. Ye, *Nature Physics* , 702 (2024).
- [42] S. L. Cornish, M. R. Tarbutt, and K. R. Hazzard, *Nature Physics* , 730–740 (2024).
- [43] D. R. Hofstadter, *Phys. Rev. B* **14**, 2239 (1976).
- [44] P. A. McClarty, M. Haque, A. Sen, and J. Richter, *Phys. Rev. B* **102**, 224303 (2020).
- [45] K. Lee, R. Melendrez, A. Pal, and H. J. Changlani, *Phys. Rev. B* **101**, 241111 (2020).
- [46] M. Creutz, *Phys. Rev. Lett.* **83**, 2636 (1999).
- [47] K. Omiya, *arXiv preprint arXiv:2601.11806* (2026).
- [48] N. O’Dea, L. Gioia, S. Moudgalya, and O. I. Motrunich, *arXiv preprint arXiv:2601.14206* (2026).
- [49] P. Weinberg and M. Bukov, *SciPost Phys.* **2**, 003 (2017).
- [50] C. Gross and I. Bloch, *Science* **357**, 995 (2017).
- [51] C. Gross and W. S. Bakr, *Nature Physics* **17**, 1316 (2021).
- [52] D. Jaksch and P. Zoller, *New Journal of Physics* **5**, 56 (2003).
- [53] E. J. Mueller, *Phys. Rev. A* **70**, 041603 (2004).
- [54] F. Gerbier and J. Dalibard, *New Journal of Physics* **12**, 033007 (2010).
- [55] M. Aidelsburger, M. Atala, M. Lohse, J. T. Barreiro, B. Paredes, and I. Bloch, *Phys. Rev. Lett.* **111**, 185301 (2013).
- [56] H. Miyake, G. A. Siviloglou, C. J. Kennedy, W. C. Burton, and W. Ketterle, *Phys. Rev. Lett.* **111**, 185302 (2013).
- [57] M. Atala, M. Aidelsburger, M. Lohse, J. T. Barreiro, B. Paredes, and I. Bloch, *Nature Physics* **10**, 588 (2014).
- [58] M. E. Tai, A. Lukin, M. Rispoli, R. Schittko, T. Menke, D. Borgnia, P. M. Preiss, F. Grusdt, A. M. Kaufman, and M. Greiner, *Nature* **546**, 519 (2017).
- [59] J. Léonard, S. Kim, J. Kwan, P. Segura, F. Grusdt, C. Repellin, N. Goldman, and M. Greiner, *Nature* **619**, 495 (2023).
- [60] A. Impertro, S. Huh, S. Karch, J. F. Wienand, I. Bloch, and M. Aidelsburger, *Nature Physics* **21**, 895–901 (2025).
- [61] P. G. Harper, *Proc. Phys. Soc. A* **68**, 874 (1955).
- [62] R. Barnett, D. Petrov, M. Lukin, and E. Demler, *Phys. Rev. Lett.* **96**, 190401 (2006).
- [63] A. V. Gorshkov, S. R. Manmana, G. Chen, E. Demler, M. D. Lukin, and A. M. Rey, *Phys. Rev. A* **84**, 033619 (2011).
- [64] K. R. A. Hazzard, S. R. Manmana, M. Foss-Feig, and A. M. Rey, *Phys. Rev. Lett.* **110**, 075301 (2013).
- [65] A. Hudomal, J.-Y. Desaulles, B. Mukherjee, G.-X. Su, J. C. Halimeh, and Z. Papić, *Phys. Rev. B* **106**, 104302 (2022).
- [66] D. Barredo, H. Labuhn, S. Ravets, T. Lahaye, A. Browaeys, and C. S. Adams, *Phys. Rev. Lett.* **114**, 113002 (2015).
- [67] S. De Léséleuc, V. Lienhard, P. Scholl, D. Barredo, S. Weber, N. Lang, H. P. Büchler, T. Lahaye, and A. Browaeys, *Science* **365**, 775 (2019).
- [68] C. Chen, G. Bornet, M. Bintz, G. Emperauger, L. Leclerc, V. S. Liu, P. Scholl, D. Barredo, J. Hauschild, S. Chatterjee, *et al.*, *Nature* **616**, 691 (2023).
- [69] G. Bornet, G. Emperauger, C. Chen, B. Ye, M. Block, M. Bintz, J. A. Boyd, D. Barredo, T. Comparin, F. Mez-zacapo, *et al.*, *Nature* **621**, 728 (2023).

- [70] C. Chen, G. Emperauger, G. Bornet, F. Caleca, B. Gély, M. Bintz, S. Chatterjee, V. Liu, D. Barredo, N. Y. Yao, et al., *Science* **389**, 483 (2025).
- [71] G. Emperauger, M. Qiao, C. Chen, F. Caleca, S. Bocini, M. Bintz, G. Bornet, R. Martin, B. Gély, L. Klein, D. Barredo, S. Chatterjee, N. Y. Yao, F. Mezzacapo, T. Lahaye, T. Roscilde, and A. Browaeys, *Phys. Rev. X* **15**, 031021 (2025).
- [72] B. Yan, S. A. Moses, B. Gadway, J. P. Covey, K. R. Hazzard, A. M. Rey, D. S. Jin, and J. Ye, *Nature* **501**, 521 (2013).
- [73] L. Christakis, J. S. Rosenberg, R. Raj, S. Chi, A. Morningstar, D. A. Huse, Z. Z. Yan, and W. S. Bakr, *Nature* **614**, 64 (2023).
- [74] J.-R. Li, K. Matsuda, C. Miller, A. N. Carroll, W. G. Tobias, J. S. Higgins, and J. Ye, *Nature* **614**, 70 (2023).
- [75] C. M. Holland, Y. Lu, and L. W. Cheuk, *Science* **382**, 1143 (2023).
- [76] Y. Bao, S. S. Yu, L. Anderegg, E. Chae, W. Ketterle, K.-K. Ni, and J. M. Doyle, *Science* **382**, 1138 (2023).
- [77] L. R. Picard, A. J. Park, G. E. Patenotte, S. Gebretsadkan, D. Wellnitz, A. M. Rey, and K.-K. Ni, *Nature* **637**, 821 (2025).
- [78] D. K. Ruttley, T. R. Hepworth, A. Guttridge, and S. L. Cornish, *Nature* **637**, 827–832 (2025).
- [79] C.-J. Lin, A. Chandran, and O. I. Motrunich, *Phys. Rev. Res.* **2**, 033044 (2020).
- [80] S. Dooley, *PRX Quantum* **2**, 020330 (2021).
- [81] N. O’Dea and A. Sriram, *Physical Review Letters* **134**, 210402 (2025).
- [82] M. Aidelsburger, M. Atala, S. Nascimbène, S. Trotzky, Y.-A. Chen, and I. Bloch, *Applied Physics B* **113**, 1 (2013).
- [83] A. Micheli, G. K. Brennen, and P. Zoller, *Nature Physics* **2**, 341 (2006).

Supplemental Information:

1. DETAILS OF EXPERIMENTAL IMPLEMENTATIONS

A. Hardcore bosons in optical lattices: THE HHBH Hamiltonian

Here we discuss the experimental implementation of the QMBS using hardcore bosons tunneling in an optical lattice under the Hofstadter-Bose-Hubbard (HHBH) Hamiltonian [43, 61]

$$\begin{aligned} \hat{H}_{\text{HHBH}} = & -J' \sum_{m,n} \left(\hat{a}_{m,n+1}^\dagger \hat{a}_{m,n} e^{i\phi_{m,n}} + \text{h.c.} \right) \\ & - J \sum_{m,n} \left(\hat{a}_{m+1,n}^\dagger \hat{a}_{m,n} + \text{h.c.} \right) \\ & + \frac{U}{2} \sum_{m,n} \hat{n}_{m,n} (\hat{n}_{m,n} - 1), \end{aligned} \quad (\text{S1})$$

Here, $J(J')$ is the effective hopping along $x(y)$, $a_{m,n}^\dagger$ ($a_{m,n}$) creates (annihilates) a boson on site $(x, y) = (m, n)$, $n_{m,n}$ is the number operator, and U is the on-site Hubbard interaction. Experimentally, the Hamiltonian in Eq. S1 is realized when the Raman lasers experience a frequency difference $\hbar(\omega_1 - \omega_2) = \Delta$, creating a running wave along the vector $\mathbf{q} = \mathbf{k}_1 - \mathbf{k}_2$ [see main text Fig. 2]. When a particle tunnels around the boundary of one square plaquette, it picks up an Aharonov-Bohm phase. With each site hosting a spatially dependent phase $\phi_{m,n} = \mathbf{q} \cdot \mathbf{r}_{m,n} = q_x d m + q_y d n$, the effective flux is therefore $\Phi = q_x d$. Appropriate choices of the angle between the Raman lasers and the frequency detuning can result in a uniform π -flux per plaquette in the ladder model. The magnitudes of J', J are functions of the bare hopping t , the phase difference between sites $\phi_{m',n} - \phi_{m,n}$, the Raman modulation amplitude, and the energy offset Δ [82]. Importantly, the relative magnitudes of J', J do not change the qualitative scar behavior, and all calculations are shown with $|J| = |J'|$. We note that this protocol's main components have already been demonstrated on previous cold atom simulators [55–60], though never in the context of quantum scars. The requirement of a finite ladder with two legs can be achieved by isolating a $2 \times L$ subsystem out of an extended two-dimensional lattice using additional barrier laser fields shaped by spatial light modulators [58]. Bosonic atomic species with tunable magnetic Feshbach resonances such as ${}^7\text{Li}$, ${}^{39/41}\text{K}$, and ${}^{133}\text{Cs}$ could be used for implementing this scar.

B. Dipolar spin-1/2 zig-zag chain

The electric dipole-dipole interaction of two particles at $\mathbf{r}_i, \mathbf{r}_j$ oriented by some external symmetry-breaking (e.g. magnetic, electric) field is given by

$$V_{\text{ddi}}(\mathbf{r}_i - \mathbf{r}_j) = \frac{d^2(1 - 3 \cos^2 \theta)}{4\pi\epsilon_0 |\mathbf{r}_i - \mathbf{r}_j|^3} \quad (\text{S2})$$

where d is the electric dipole moment and θ parametrizes the angle between the quantization axis and the separation $\mathbf{r}_i - \mathbf{r}_j$. We consider a system where the dipoles' translational motion is frozen in a deep optical tweezer array. Consider two internal states $|\downarrow\rangle, |\uparrow\rangle$ that represent opposite-parity states coupled by an electric dipole transition matrix element. In the absence of an external static electric field, the two-level system can be described with a lattice spin-exchange model [62–64]

$$\hat{H}_{\text{SE}} = \sum_{i>j} \frac{J_{ij}}{2} \left(\hat{S}_i^+ \hat{S}_j^- + \hat{S}_i^- \hat{S}_j^+ \right) \quad (\text{S3})$$

with the exchange interaction J_{ij} given by the dipole-dipole interaction in Eq. S2, and S_i^\pm are the spin-1/2 operators on site i . This Hamiltonian physically represents the transfer of the spin excitation between two particles; since a particle may not be doubly-excited, the spin excitation can be mapped to a hardcore boson. The zig-zag chain with carefully chosen angles is a crucial ingredient to recover the phenomenology of the QMBS of Eq. 1. Reconfigurable optical tweezer arrays allow for high tunability of couplings in an electric dipolar system. By appropriate choice of quantization axis and the angles α, β , we can ensure that the diagonal coupling terms J_{orange} and J_{blue} are equal in

magnitude but opposite in sign (see Fig. 3c), fulfilling the kinetic frustration condition of destructive interference in analogy to the model in Fig. 1a.

For state preparation of $|\psi\rangle_{\text{scar}}$, we can start from a unit-filled array of $|\downarrow\rangle$. The initial state can be prepared by selective excitation of the appropriate sites (1, 3, 5 ...) to $|\uparrow\rangle$ with microwaves, either in tweezers in a separate region which are then moved into position on the zig-zag chain, or directly in the target region along with site-selective dressing beams that provide local ac Stark shifts to isolate target sites for excitation.

Our proposal of the dipolar XY quantum many-body scar can be implemented in existing Rydberg and polar molecule quantum simulators. Rydberg atoms trapped in optical tweezer arrays are a leading platform for studying quantum many-body dynamics [40], and they can encode an effective spin-1/2 as opposite parity angular momentum states, *e.g.*, $|\uparrow\rangle = |nS\rangle$ and $|\downarrow\rangle = |nP\rangle$, where n is a high principal quantum number. Thus they realize resonant dipolar interactions, which have already been utilized in several experiments [66–71]. The electric dipole moment d in Eq. S2 is given by the matrix element between $|\uparrow\rangle, |\downarrow\rangle$, and an external magnetic field sets the quantization axis. The magnetic field can also isolate $|\uparrow\rangle, |\downarrow\rangle$ from irrelevant Zeeman sublevels. The resonant dipolar interactions lead to nearest-neighbor couplings $J \approx h \times 0.1 - 10$ MHz at typical 10 - 20 μm separations. Decoherence primarily stems from finite Rydberg lifetimes ($\sim 100 \mu\text{s}$ at room temperatures) and finite position distributions due to thermal motion ($\sigma_r \sim 100, \sigma_z \sim 800$ nm radially or axially in the tweezer) [70]. An estimate of these decoherence effects on the ideal approximate scar conditions show that the QMBS visibility still persists out to many oscillations (see Section 6).

In addition to Rydberg atoms, ultracold polar molecules are capable of realizing our model. Polar molecules are emerging as a powerful quantum technology combining tunable interactions, rich internal structures, and long-lived coherence times [41, 42]. Heteronuclear molecules possess permanent body-frame electric dipole moments of order 0.1-10 Debye, and their rotational levels $|N, m_N\rangle$ are strongly coupled through dipole-dipole interactions, where N is the rotational quantum number and m_N is its projection onto the quantization axis. Within one electronic and vibrational level, molecules can form an isolated two-level system between $|\uparrow\rangle = |N=0, m_N=0\rangle$ and any of $|1, 0\rangle$ or $|1, \pm 1\rangle$ for $|\downarrow\rangle$. The molecules are governed by the spin-exchange Hamiltonian of Eq. S3 [62, 63, 83], as long as degeneracies between molecular nuclear spin states are lifted sufficiently to isolate the 2-level system (by nuclear quadrupole moments or by Zeeman shifts). The spin-exchange Hamiltonian has been studied in lattice [72–74] and optical tweezer [75–78] systems, and extension to our model with a dipolar zig-zag chain is straightforward. Compared to Rydbergs, the nearest-neighbor J of polar molecules is weaker (ranging from $h \times 10$ Hz - 10 kHz levels at $\sim 1 \mu\text{m}$ distances), but molecules benefit from long-lived coherence times of up to $\tau_2 \approx 10$ s [78], enabling decoherence-limited quality factors theoretically up to $J\tau_2 \approx 10^5$. However, state-preparation of large-scale defect-free molecular tweezer arrays is still an outstanding challenge.

2. LEVEL SPACING DISTRIBUTION FOR PERIODIC BOUNDARY CONDITIONS

Here we give additional details on the level spacing distribution, which indicates non-integrability of our model. For the original model of Eq. 1 with periodic boundary conditions, label P_y as the inversion along the y axis, F as the Z flip symmetry, and P'_x as inverting the top and bottom chain, and add π phases to all the odd rungs. Next nearest neighbor interactions t_{nn} introduced in the End Matter will break P'_x so here we use the next-next neighbor interactions t_{nnn} instead. t_{nnn} preserves all symmetries and keeps the scar exact. We found that $\langle r \rangle$ has a dip compared to the value predicted by the Wigner-Dyson distribution at $t_{nnn} = 0$ (which is the model of Eq. 1) and as L grows, the dip becomes smaller, shown in Fig. S1(a). To investigate whether the dip is due to the finite system effect, we also calculate $\langle r \rangle$ in $N_{\text{up}} = 6$ sector, where the Hilbert space dimension is greatly reduced and larger system sizes become accessible. In this sector, $\langle r \rangle$ increases with L and at $L = 18$, $\langle r \rangle = 0.515$, which is close to Wigner-Dyson distribution, shown in Fig. S1(b). Taken together, these data suggest that in the thermodynamic limit, our model with $t_{nnn} = 0$ is non-integrable.

3. DETAILS ABOUT FITTING IN FIGURE 4

The scar lifetime τ in Fig. 4 is calculated by fitting the imbalance oscillation with time. The function used for fitting is

$$f(t) = A \cos(\Omega t + \phi) \exp(-t/\tau) \quad (\text{S4})$$

where A, Ω, ϕ and τ are free fit parameters. For bosonic lattice, the oscillation first decay and then revive, which is largely due to the finite system sizes. In order to minimize the finite system size effect, we choose the time that the oscillation amplitude reaches the first minimum as the end point of fitting. For dipolar spin chain, since the oscillation

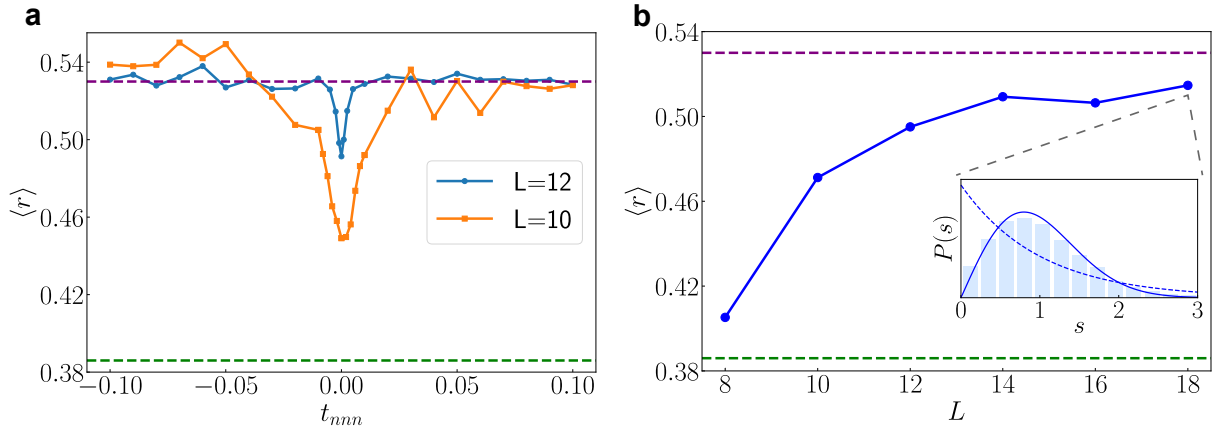


FIG. S1. **Nearest neighbor spacing ratio with t_{nnn} and L .** (a) $\langle r \rangle$ value in $S_z = 0, K_x = 0, P_y = 1, P'_x = 1, F = 1$ sector. t_{nnn} is the next-next nearest neighbor hopping strength. The purple and green dashed lines indicate $\langle r \rangle$ for Wigner-Dyson and Poissonian distributions, respectively. (b) $\langle r \rangle$ value in $N_{\text{up}} = 6, K_x = 0, P_y = 1, P'_x = 1$ sector for different system size for $t_{nnn} = 0$. The inset shows the level spacing distribution for $L = 18$. Blue and dashed blue curve in the inset correspond to Wigner-Dyson and Poisson distributions, respectively.

amplitude never revive, we simply choose a cutoff at $J_0 t = 40$. The fitting results for all the data points in Fig. 4 of the main text are shown in Fig. S2. The error bar of τ is smaller than the size of the point and thus is not shown.

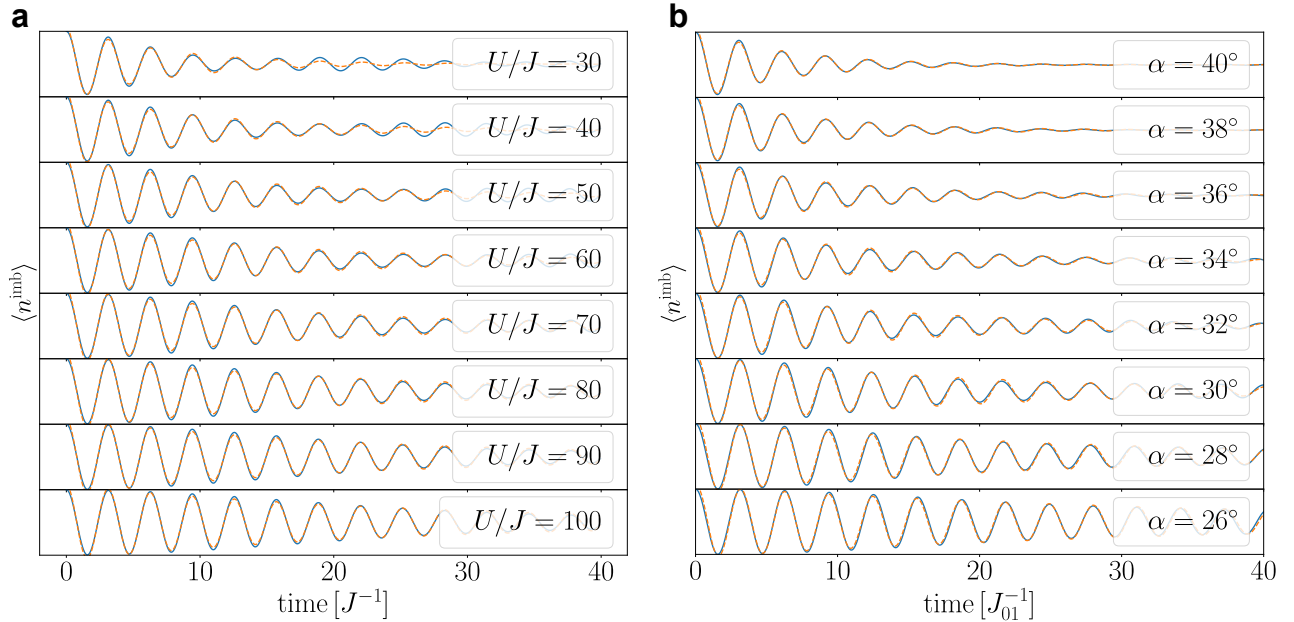


FIG. S2. **Lifetime fitting details for Fig. 4 of the main text.** Subfigure (a) shows the fitting results for optical lattice with different $U/|J|$ while (b) shows the results for dipolar spin chain under different α . The blue curve is the simulated data from QuSpin and the yellow curve is the fit from Eq. S4.

4. FINITE SYSTEM SIZE EFFECT

Due to limited computational resources, the system size accessible to numerical simulations in QuSpin is limited to around $L = 10$, where boundary effects may have an influence on the result.

For the time evolution results, we found that the initial time evolution is largely independent of system size, while for later time, the evolution is more sensitive. In order to test whether the results can be extended to even larger

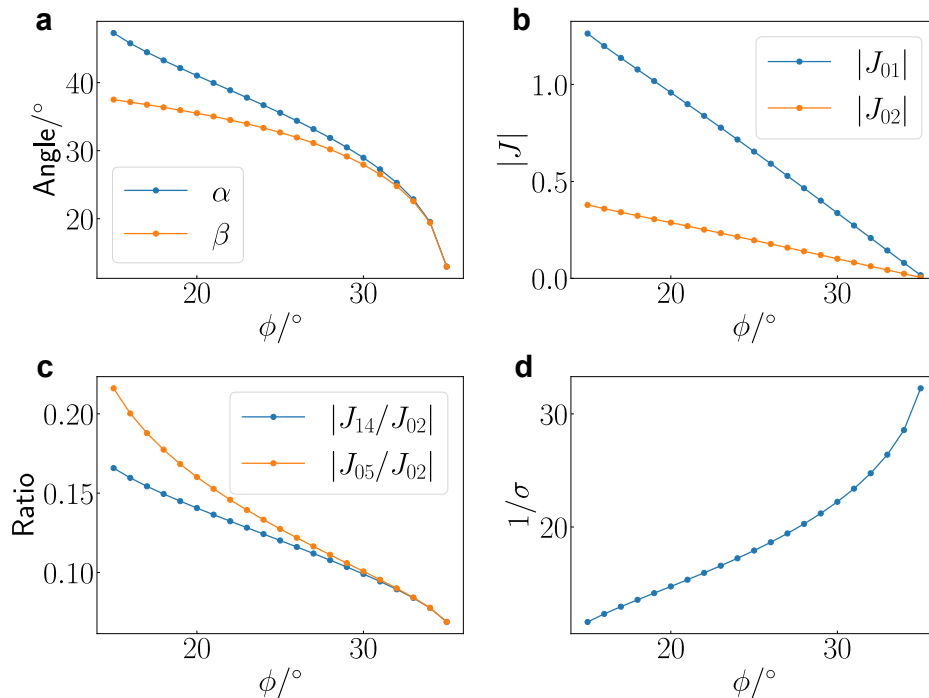


FIG. S3. **Optimizing the scar lifetime for a dipolar spin chain.** Different parameters with respect to ϕ for a fixed $J_{02}/J_{01} = 0.3$. (a) α and β values for realizing the model. (b) Long range interactions decrease with ϕ . (c) Absolute value of the interaction strength decreases with ϕ . (d) The estimated scar lifetime $1/\sigma$ with ϕ where σ is calculated using the same method as in Fig. 4.

system, we compute the time evolution of exactly same parameters under different system sizes [see Fig. S4]. If the results are mostly the same for different system sizes, we believe it is a property that can be generalized to infinite size chain.

5. OPTIMIZING QMBS IN DIPOLAR SPIN CHAINS

For a zigzag chain system, there are 5 degrees of freedom: the distance between site 0 and 1, α, β , and the polar and azimuthal angles of the quantization axis. For the quantum many-body scar, there are two constraints: $J_{03} = 0$ and $J_{02} + J_{13} = 0$. Also, we want to fix the ratio of J_{02}/J_{01} so that the model is completely determined. The distance between site 0 and 1 corresponds to an overall scaling of the interaction strength, which does not change the dynamical properties of the system. In the end, there is one degree of freedom for us to optimize, which we choose to be ϕ , where ϕ is the angle between quantization axis and the plane. Here we demonstrate the optimization for $J_{02}/J_{01} = 0.3$. Results are shown in Fig. S3. As ϕ increases, the long range term J_{14}, J_{05} decreases, but at the same time, the absolute value of the interaction decreases (set $r_{01} = 1$, where r_{01} is the distance between site 0 and 1). Ideally, we can keep increasing ϕ to reach a minimum strength of long range interactions. However, in a realistic experiment, we need to balance between minimizing long range interactions and keeping sufficiently high absolute interaction strengths.

6. LEAKAGE OF QMBS DUE TO EXPERIMENTAL LIMITATIONS AND ERRORS

1. Optical Lattice

For state-of-the-art optical lattice experiments, possible errors include flux inhomogeneity and disorder in the chemical potential. We estimate the effects of these disorders in Fig. S5.

Disorder in the chemical potential: We assume a Gaussian distribution of chemical potentials in the lattice sites,

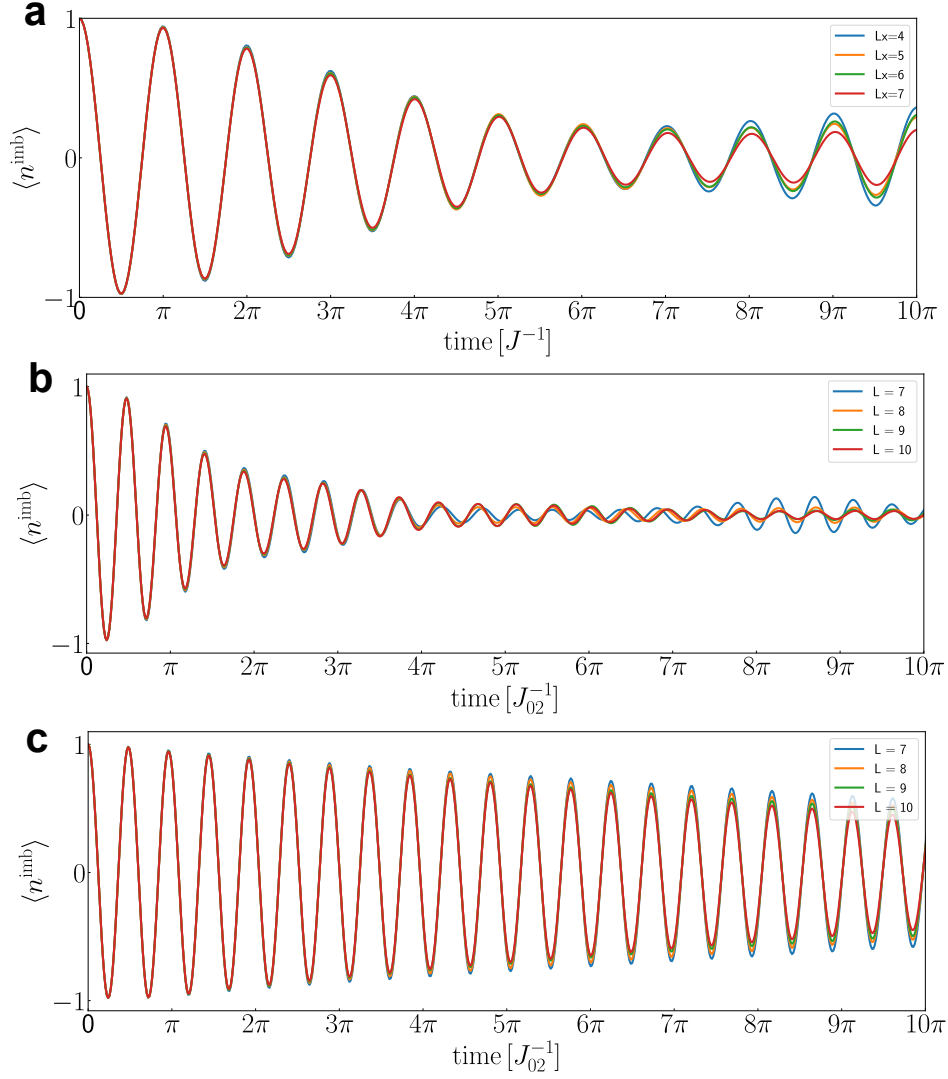


FIG. S4. **Finite size effect on time evolution in Fig. 2 and Fig. 3 of the main text.** Here we show the imbalance dynamics of different system sizes under the same Hamiltonian. (a) Time evolution of imbalance under $U/J = U/J' = 50$ with bosonic lattice Hamiltonian. (b)(c) Time evolution of imbalance with the same configuration as in Fig. 3c without and with Floquet driving.

with $\sigma = J/5$ and take $U/J = 50$ for all simulations. The simulation is carried out in a $L = 7$ ladder.

Flux deviation: We assume the flux is uniform across the ladder but has an overall deviation from π . The simulation is carried out with $U/J = 50$ in a $L = 7$ ladder.

2. Rydberg atoms array

A dominant error in dipolar tweezer array experiments is positional disorder, whose effect is magnified when tweezers are moved closer to each other. We estimate the wavepacket spread of a single particle to be $\sigma_r = 100$ nm, $\sigma_z = 800$ nm, in the radial (in-plane) and axial (out-of-plane) directions respectively, and we set the distance between site 0 and 1 to $15\mu\text{m}$. We simulate the results with 3 sets of parameters in a $L = 10$ ladder. Fig. S6 shows the imbalance dynamics averaged over multiple shots in the presence of positional disorder. We also note that for dipolar interactions C_3/r^3 , further spacing the tweezers apart at the expense of reducing all J couplings is one route to suppressing the effect of disorder.

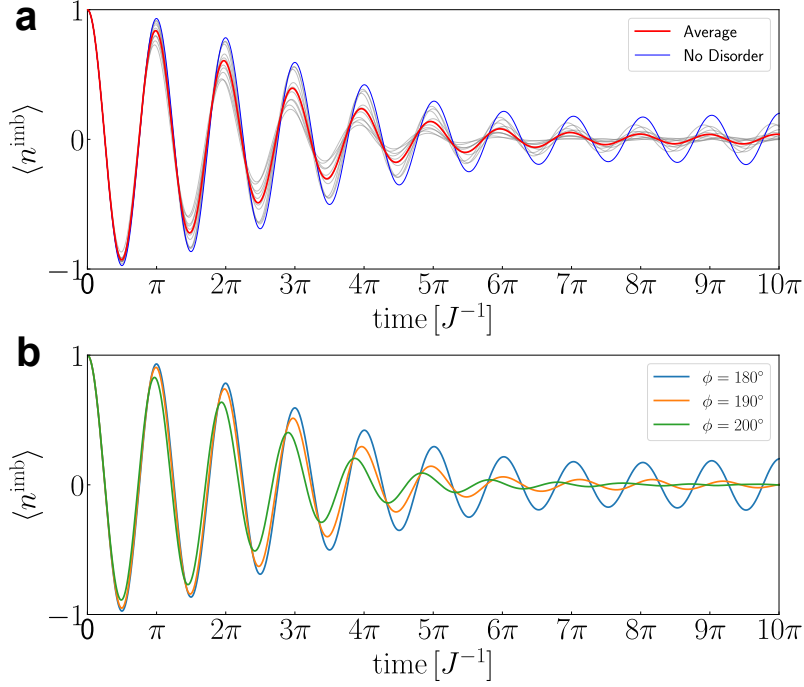


FIG. S5. **(a)** Scarring dynamics for hardcore bosons on a π -flux ladder, with disorder in the chemical potential. The red curve shows the ideal case, where disorder is set to zero. The grey lines show the dynamics with a Gaussian distribution of chemical potentials [see text]. **(b)** Scarring dynamics with deviations to the $\phi = \pi$ phase for hardcore bosons in an optical π -flux lattice. The legend indicates the phase.

7. FIDELITY AND IMBALANCE

Here we would like to show the analytical expression of these two quantities and how to understand them. For a L site chain, there are $L + 1$ exact scar eigenstates, labeled as $|\psi_n\rangle$. The QMBS initial state can be written as $|\psi_{\text{QMBS}}\rangle = \sum_n a_n |\psi_n\rangle$. With static imperfections like long range interactions, $|\psi_n\rangle$ splits into several other states. Label the new eigenstates $|\psi_{n\alpha}\rangle$ and write $|\psi_n\rangle = \sum_\alpha b_{n\alpha} |\psi_{n\alpha}\rangle$. Define $\rho_{n\alpha} \equiv |b_{n\alpha}|^2$. The fidelity is simply given by

$$F(t) = \left| \sum_{\alpha,n} a_n^2 \rho_{n\alpha} e^{-iE_{n\alpha}t} \right|^2 \quad (\text{S5})$$

For the imbalance, notice that $\langle n^{\text{imb}} \rangle = \frac{1}{L}(J^+ + J^-)$. The averaged value of imbalance is given by

$$\langle n^{\text{imb}} \rangle(t) = \frac{1}{L2^{L-1}} \sum_{n=0}^{L-1} \sum_{\alpha,\beta} \frac{L!}{n!(L-n-1)!} \rho_{n\alpha} \rho_{n+1,\beta} \cos(E_{n\alpha} - E_{n+1,\beta})t \quad (\text{S6})$$

8. SCAR LIFETIME WITH PERTURBATION STRENGTH

Here we investigate the relationship between scar lifetime and perturbation strength. The lifetime is estimated using the energy width σ introduced in the main text. For bosonic lattice, the first order perturbation is $\begin{bmatrix} 0 & 0 \\ 1 & 1 \end{bmatrix} \rightarrow \begin{bmatrix} 0 & 0 \\ 0 & 2 \end{bmatrix} \rightarrow \begin{bmatrix} 0 & 0 \\ 1 & 1 \end{bmatrix}$, with the perturbation strength $\delta V \propto J^2/U$. For dipolar spin chain, the perturbation terms are longer range interactions, with strength $\delta V \propto (|J_{14}| + |J_{05}|)/|J_{02}|$. The parameters for dipolar spin chain are from Fig S2. We found that the lifetime τ proportional to $1/\delta V$ in both cases in Fig. S7.

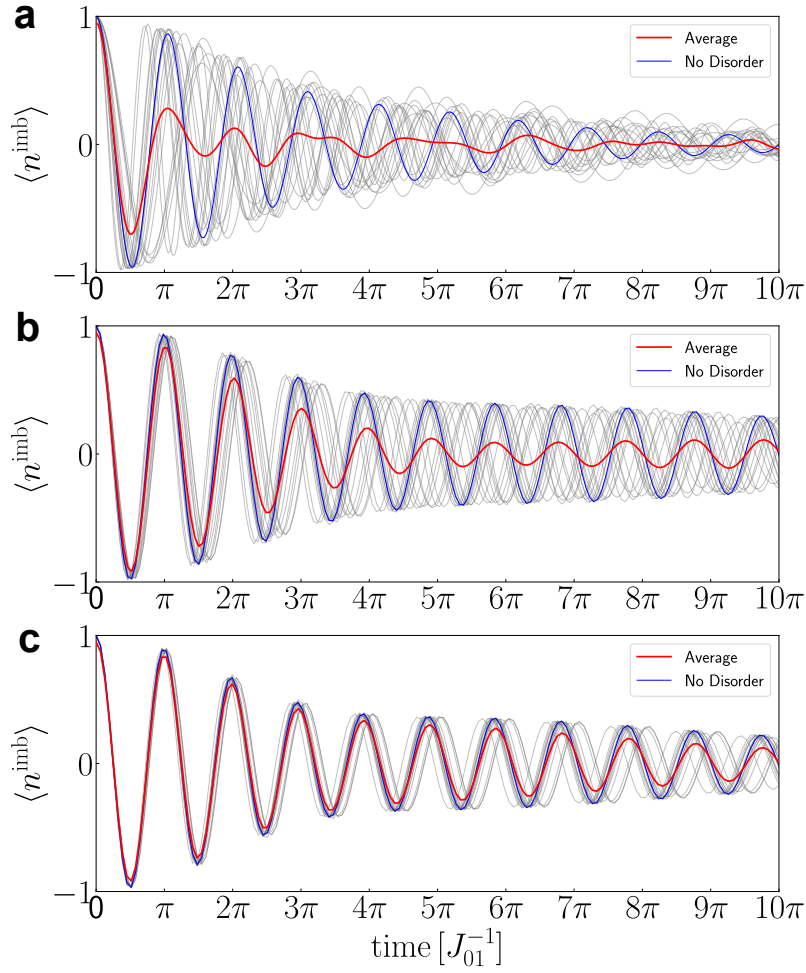


FIG. S6. **Scarring dynamics for dipolar spin chain in the presence of positional disorder.** The gray curves show the results for individual runs of the experiment, *i.e.*, different instances of random positional disorder. The red curves show the time evolution results averaged over 19 shots, and the blue curve shows the ideal result without disorder. **(a)(b)(c)** correspond to different configurations. **(a)** $\phi = 30^\circ, \alpha = 34^\circ, J_{02}/J_{01} = 0.480$. **(b)** $\phi = 15^\circ, \alpha = 44^\circ, J_{02}/J_{01} = 0.275$. **(c)** $\phi = 0^\circ, \alpha = 52.49^\circ, J_{02}/J_{01} = 0.248$.

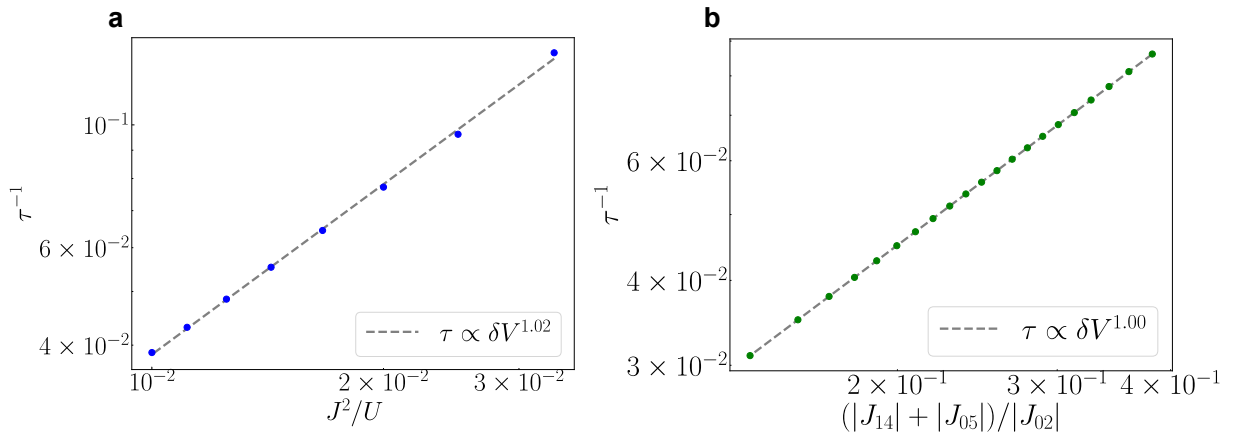


FIG. S7. **Scar lifetime with perturbation strength** **(a)** Inverse lifetime τ^{-1} with $\delta V = J^2/U$. An exponent of 1.022 ± 0.013 was derived from logarithmic fitting. **(b)** Inverse lifetime τ^{-1} with δV . The exponent is 1.0013 ± 0.0001 .